

**Polydisperse Versus Monodisperse Microbubbles  
A Simulation Study for Contrast-Enhanced Ultrasound Imaging**

Matalliotakis, Agisilaos; Verweij, Martin D.

**DOI**

[10.1016/j.ultrasmedbio.2024.11.002](https://doi.org/10.1016/j.ultrasmedbio.2024.11.002)

**Publication date**

2025

**Document Version**

Final published version

**Published in**

Ultrasound in Medicine and Biology

**Citation (APA)**

Matalliotakis, A., & Verweij, M. D. (2025). Polydisperse Versus Monodisperse Microbubbles: A Simulation Study for Contrast-Enhanced Ultrasound Imaging. *Ultrasound in Medicine and Biology*, 51(3), 452-462. <https://doi.org/10.1016/j.ultrasmedbio.2024.11.002>

**Important note**

To cite this publication, please use the final published version (if applicable).  
Please check the document version above.

**Copyright**

Other than for strictly personal use, it is not permitted to download, forward or distribute the text or part of it, without the consent of the author(s) and/or copyright holder(s), unless the work is under an open content license such as Creative Commons.

**Takedown policy**

Please contact us and provide details if you believe this document breaches copyrights.  
We will remove access to the work immediately and investigate your claim.



## Original Contribution

## Polydisperse Versus Monodisperse Microbubbles: A Simulation Study for Contrast-Enhanced Ultrasound Imaging

Agisilaos Matalliotakis<sup>a</sup>, Martin D. Verweij<sup>a,b,\*</sup><sup>a</sup> Section of Medical Imaging, Department of Imaging Physics, Faculty of Applied Sciences, Delft University of Technology, Delft, The Netherlands<sup>b</sup> Section of Biomedical Engineering, Department of Cardiology, Erasmus University Medical Center, Rotterdam, The Netherlands

## ARTICLE INFO

## Keywords:

Contrast-enhanced ultrasound  
 Deep tissue imaging  
 Microbubbles  
 Monodisperse  
 Polydisperse  
 Non-linear oscillations  
 Multiple scattering  
 Non-linear imaging artifacts  
 INCS  
 Acoustic simulations

## ABSTRACT

**Objective:** Contrast-enhanced ultrasound (CEUS) presents distinct advantages in diagnostic echography. Utilizing microbubbles (MBs) as conventional contrast agents enhances vascular visualization and organ perfusion, facilitating real-time, non-invasive procedures. There is a current tendency to replace traditional polydisperse MBs with novel monodisperse formulations in an attempt to optimize contrast enhancement and guarantee consistent behavior and reliable imaging outcomes. This study investigates the contrast enhancement achieved using various-sized monodisperse MBs and their influence on non-linear imaging artifacts observed in traditional CEUS.

**Methods:** To explore the differences between monodisperse and polydisperse populations without excessive experimentation, numerical simulations are employed for delivering precise, objective and expeditious results. The iterative non-linear contrast source (INCS) method has previously demonstrated efficacy when simulating ultrasound propagation in large populations in which each bubble has individual properties and several orders of multiple scattering are significant. Therefore, this method is employed to realistically simulate both monodisperse and polydisperse MBs.

**Results:** Our findings in CEUS imaging indicate that scattering from resonant monodisperse MBs is 11.8 dB stronger than scattering from polydisperse MBs. Furthermore, the amplitude of non-linear imaging artifacts downstream of the monodisperse population is 19.4 dB stronger compared with polydisperse suspension.

**Conclusion:** Investigating the impact of multiple scattering on polydisperse populations compared with various monodisperse suspensions has revealed that monodisperse MBs are more effective contrast agents, especially when at resonance. Despite the strong signal-to-noise ratio of monodisperse populations, imaging artifacts caused by non-linear wave propagation are also enhanced, resulting in further mis-classification of MBs as tissue.

## Introduction

Achieving superior deep tissue imaging of blood vessels with ultrasound remains a challenge in medical diagnostics but contrast-enhanced imaging, particularly using microbubbles (MBs), has emerged as a promising solution [1,2]. These gas-filled microspheres, stabilized with a lipid or protein shell, enhance blood contrast for improved organ and lesion visualization. MBs, characterized by their small size, biocompatibility and vascular navigability, resonate in the ultrasound frequency range (1–10 MHz). Their efficient sound scattering in both fundamental and harmonic modes, driven by substantial acoustic impedance differences with their surroundings and highly non-linear oscillatory behavior [3,4], enhances image quality. As ultrasound waves propagate through a resonant MB suspension, they undergo non-linear distortion due to non-linear MB scattering influenced by size, shell characteristics, ultrasound pressure and frequency [5–7]. Due to these properties, MBs have also been demonstrated to be efficient contrast agents in various applications

in addition to contrast-enhanced ultrasound (CEUS), such as ultrasound localization microscopy [8].

As a drawback, wave distortion can extend beyond an MB suspension, leading to the mis-identification of tissues as MBs and diminishing the specificity of CEUS imaging [9]. Narrowing the size distribution of the MB population could be a way to provide improved acoustic scattering, reduce imaging artifacts and enhance scattering homogeneity. Historically, polydisperse MBs of varying size distributions (typical radii 0.5–15 μm) have been standard in ultrasound contrast imaging [10,11]. Recent technological breakthroughs have introduced the possibility of using monodisperse, *i.e.*, uniformly sized, MBs [12]. Studies have highlighted the superiority of monodisperse MBs [13], offering enhanced predictability, improved acoustic performance and clearer imaging signals [14,15]. Nevertheless, we believe that it is important to shed more light on the effect of monodisperse MBs as contrast agents for deep vessel imaging, particularly for the generation of clearer echoes and reducing imaging artifacts.

\* Corresponding author. Lorentzweg 1, 2628CJ, Delft, The Netherlands.

E-mail address: [m.d.verweij@tudelft.nl](mailto:m.d.verweij@tudelft.nl) (M.D. Verweij).<https://doi.org/10.1016/j.ultrasmedbio.2024.11.002>

Received 13 May 2024; Revised 1 November 2024; Accepted 3 November 2024

The use of computational tools is an efficient way to perform comprehensive investigations without performing extensive measurements. Initially, studies focused on the collective behavior of bubbly media for marine applications [16,17]. Effective medium theory facilitated 1-D computational studies for both monodisperse [18,19] and polydisperse [20,21] MB suspensions in medical ultrasound, including high-intensity focused ultrasound [22]. Previous models successfully captured non-linear ultrasound propagation through uniform MB distributions in 2-D using iterative schemes [23,24]. Challenges have arisen when coupling the non-linear dynamics of multiple MBs in 3-D realistic simulations due to the complexity of the coupled Rayleigh-Plesset equation [25]. Another difficulty is when the number of polydisperse MBs is small and the use of averaged quantities becomes questionable. Various computational methods have been explored to understand the dynamics between polydisperse and monodisperse MB populations. Among these, the iterative non-linear contrast source (INCS) method has demonstrated efficacy in simulating bubble cloud behavior in a 3-D domain when excited either by a plane wave or a focused beam. This method enables the generation and comparison of echoes produced by dense monodisperse MB populations, taking into account multiple scattering [26]. This is crucial for optimizing CEUS applications and reducing the need for excessive experimentation.

The aim of this numerical study is to investigate the efficacy of monodisperse and polydisperse populations when used as contrast agents for deep tissue imaging. More precisely, this article discusses an extension of the INCS method to simulate the behavior of a population of polydisperse scatterers.

Furthermore, the effectiveness of the extended INCS method is illustrated by simulating the multiple scattering that occurs inside a population of polydisperse MBs, each with individual properties represented by its own Marmottant model [4]. INCS is based on an iterative scheme for computing the scattered acoustic signals [27,28]. Numerically, the accuracy of the final result improves after each iteration. In a physical sense, each iteration adds an extra order of multiple scattering corresponding to an additional path of wave propagation.

First, in the ‘Inclusion of a polydisperse MB population’ section below, the fundamental theory behind the INCS method is explained, followed by its extension with the introduction of polydisperse point scatterers. In the section ‘Configurations used in the simulations,’ configurations for the numerical experiments are discussed. Next, in the ‘Numerical results’ section, the results from the numerical simulations for each different test case are presented. Concluding remarks are given in the ‘Conclusion’ section.

## Inclusion of a polydisperse MB population

### Linear field

The linear pressure field generated by an external source in a linear, lossless, homogeneous acoustic background medium is described by the wave equation (eqn [1]):

$$c_0^{-2} \frac{\partial^2 p(x, t)}{\partial t^2} - \nabla^2 p(x, t) = S_{\text{pr}}(x, t) \quad (1)$$

Here,  $\mathbf{x}$  [m] is the Cartesian position vector and  $t$  [s] is the time. Furthermore,  $p(x, t)$  [Pa] is the acoustic pressure and  $c_0 = 1/\sqrt{\rho_0 \kappa_0}$  [m/s] is the small signal sound speed in the background medium, where  $\rho_0$  [kg·m<sup>-3</sup>] is the mass density and  $\kappa_0$  [Pa<sup>-1</sup>] is the compressibility. The symbol  $\nabla^2$  indicates the Laplacian operator. The acoustic field is generated by the primary source term,  $S_{\text{pr}}$  (eqn [2]):

$$S_{\text{pr}}(x, t) = \rho_0 \frac{\partial q(x, t)}{\partial t} - \nabla \cdot \mathbf{f}(x, t) \quad (2)$$

where  $q(x, t)$  [s<sup>-1</sup>] is the volume density of the volume injection rate and  $\mathbf{f}(x, t)$  [N/m<sup>3</sup>] is the volume force density of the external source. A source with a plane aperture, e.g., a phased array transducer, can be represented

by a pressure jump in the particle velocity or pressure. This can formally be described by a primary source term with a Dirac delta function [27], but in our numerical implementation of INCS, the source was modeled as a boundary condition at the location of the source aperture.

### Non-linear field due to contrast agents

In medical ultrasound, non-linearities arising from contrast media can have a significant impact on the propagation of the acoustic signals. To incorporate any phenomena that affect the pressure field, we extended eqn (1) with a contrast source term,  $S_{\text{cs}}$  (eqn [3]):

$$c_0^{-2} \frac{\partial^2 p}{\partial t^2} - \nabla^2 p = S_{\text{pr}} + S_{\text{cs}}(p). \quad (3)$$

With this approach, multiple contrast sources can be accommodated that represent global non-linear effects [27,28], attenuation [29,30], non-homogeneous medium properties [31] or local non-linear effects [32]. In contrast-enhanced imaging, the non-linear oscillatory behavior of the MBs influences the pressure field. To include the contribution of a population of a total number  $N$  of MBs, each was described as a point scatterer and the source term was written as eqn (4) [26]:

$$S_{\text{cs}}(x, t) = \sum_{i=1}^N S_{\text{MB}_i} \delta(\mathbf{x} - \mathbf{x}_{\text{sc}}^{(i)}) \\ = \rho_0 \sum_{i=1}^N \frac{d^2 V^{(i)}(\mathbf{x}_{\text{sc}}^{(i)}, t)}{dt^2} \delta(\mathbf{x} - \mathbf{x}_{\text{sc}}^{(i)}) \quad (4)$$

where  $V^{(i)}$  [m<sup>3</sup>] is the volume of the  $i$ th MB,  $\mathbf{x}_{\text{sc}}^{(i)}$  is the position vector of its center and  $\delta(\mathbf{x} - \mathbf{x}_{\text{sc}}^{(i)}) = \delta(x - x_{\text{sc}}^{(i)}) \delta(y - y_{\text{sc}}^{(i)}) \delta(z - z_{\text{sc}}^{(i)})$  [m<sup>-3</sup>] is the 3-D Dirac delta distribution. Each scatterer’s volume depends on the bubble radius,  $R$ , as a function of time, which in our case was calculated by solving the Marmottant equation [4,26].

In the case of a population of monodisperse MBs, the equilibrium radius,  $R_0$ , is the same for all the scatterers, whereas for a polydisperse distribution, each scatterer has its own  $R_0, R_0^{(i)}$ .

## Configurations used in the simulations

### Simulation of pressure fields

#### Incident field and contrast domain

To study the influence of different populations of MBs on a propagating plane wave, we considered the computational domain and the domain for the contrast media, as depicted in Figure 1a. This configuration is used in sections ‘Comparison of INCS and effective medium theory’ and ‘Plane wave: monodisperse vs polydisperse populations’ for INCS validation and the comparison between different populations, respectively. Computational domain dimensions  $X \times Y \times Z = 20 \text{ mm} \times 20 \text{ mm} \times 30 \text{ mm}$  were used. The scatterers were placed in a domain with dimensions  $X \times Y \times Z = 15 \text{ mm} \times 15 \text{ mm} \times 4.444 \text{ mm}$ , resulting in 1 mL volume. These configuration choices were made to simplify the comparison between polydisperse and monodisperse populations.

The incident pressure field is a plane wave being generated at  $z = 0$  and propagating in the positive  $z$ -direction. A plane wave is used to initially excite all the scatterers by an incident wave that has the same pressure amplitude everywhere. The temporal signature of the incident pressure is given as (eqn [5]):

$$p(t) = P_0 \exp \left[ -\left( \frac{t - T_d}{T_w/2} \right)^2 \right] \sin[2\pi f_0(t - T_d)], \quad (5)$$

where  $T_w = 3/f_0$  is the width and  $T_d = 6/f_0$  is the delay of a Gaussian envelope with a duration of  $12/f_0$ , where  $f_0 = 1 \text{ MHz}$  is the center frequency. Therefore, this is a narrow-band pulse. The peak pressure is  $P_0 = 200 \text{ kPa}$ . The scatterers were embedded in water with a density of

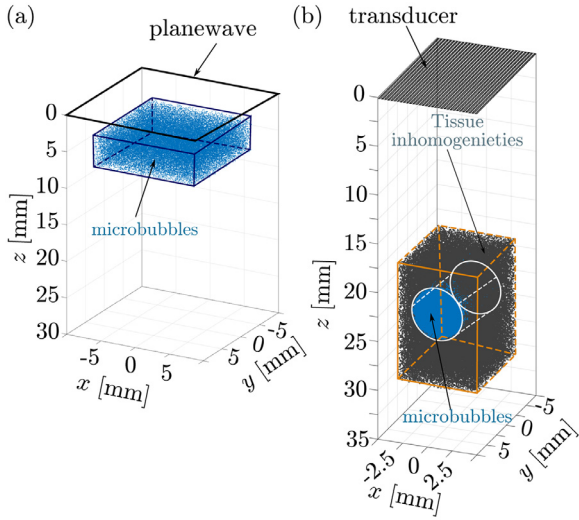


**Figure 1.** Configurations used in the iterative non-linear contrast source simulations. (a) Computational domain containing a suspension of  $3.5 \times 10^4 \text{ mL}^{-1}$  (blue) monodisperse microbubbles (MBs) with a  $3.2 \mu\text{m}$  equilibrium radius, embedded in water. (b) Computational domain incorporating  $7 \times 10^5 \text{ mL}^{-1}$  tissue-mimicking linear scatterers (gray) surrounding a suspension of  $5 \times 10^5 \text{ mL}^{-1}$  monodisperse MBs with a  $1.4 \mu\text{m}$  equilibrium radius (blue).

$\rho_0 = 1060 \text{ kg/m}^3$  and a speed of sound of  $c_0 = 1482 \text{ m/s}$ . In the considered situations, water had negligible losses and non-linear effects were hardly noticeable. Therefore, we assumed that the embedding medium was lossless and linear. A sampling frequency of 18 MHz was used as the basis for the discretization of the spatiotemporal domain [26].

#### Configuration for validation

To validate INCS, we compared our results with those following effective medium theory. Analytical expressions describing the effective behavior of a population of isotropic linear scatterers (LSs) were derived from Foldy [16,17]. A similar validation was used in a previous publication for a monodisperse population of scatterers [26], but here we considered a polydisperse population. For INCS implementation, we assumed that the contrast source term for each LS is given by eqn (6):

$$S_{sc}(\mathbf{x}, t) = -f(R_0)V_0 \frac{\rho_0}{\rho_1 c_1^2} \frac{\partial^2 p(\mathbf{x}_{sc}, t)}{\partial t^2} \delta(\mathbf{x} - \mathbf{x}_{sc}), \quad (6)$$

where  $R_0$  is the equilibrium radius,  $V_0$  is its initial volume,  $\rho_1$  is the density of mass of the gas inside the LS,  $c_1$  is the speed of sound inside the LS and  $f(R_0)$  is the polydispersity co-efficient given by eqn (7):

$$f(R_0) = \frac{A_0}{(R_0/R_{0,ref})^\gamma}. \quad (7)$$

The constant  $A_0$  was used to adjust the scattering strength if necessary and  $\gamma$  was the polydispersity scale parameter to control the scattering distribution of the population.

In the case of a plane wave excitation as in eqn (5), the scattered pressure was given by eqn (8) [26]:

$$\begin{aligned} p_{sc}(\mathbf{x}, \omega) &= f(R_0)V_0 \frac{\rho_0}{\rho_1 c_1^2} \omega^2 \frac{p(\omega)}{4\pi r} e^{-ikr} \\ &= g(R_0\omega) \frac{p(\omega)e^{-ikr}}{r}, \end{aligned} \quad (8)$$

where  $k = \omega/c_0$  is the wavenumber,  $g(R_0, \omega)$  is the scattering strength of an individual LS, and  $r$  is the distance from the scatterer. We followed this approach to match the variables, as defined previously by Foldy [16].

For the linear isotropic scatterers under consideration, we chose the scattering strength to be a linear function of the (fictitious) radius of a scatterer, instead of its (fictitious) volume. In this way, we avoided the

extreme dominance of the larger bubbles in the polydisperse population. This was achieved by setting  $\gamma = 2$  in eqn (7). To ensure that INCS yielded convergent results under the considered circumstances, we assumed that  $A_0 = 0.6$  and  $R_{0,ref} = 1 \mu\text{m}$ .

For the polydisperse populations considered in this paper, the density of the MBs varied with the  $R_0$  according to the gamma distribution (eqn [9]):

$$n(R_0) = \frac{N}{V} \frac{1}{b^\alpha \Gamma(\alpha)} R_0^{\alpha-1} e^{-R_0/b}, \quad (9)$$

where  $N$  is the total number of scatterers and  $V$  is the volume in which the homogeneous population resides. Furthermore,  $\alpha$  and  $b$  are the scale and shape parameters, and  $\Gamma$  is the gamma function [33]. In this paper, we chose  $\alpha = 2.24$  and  $b = 1.23 \mu\text{m}$  to mimic the size distribution of Optison [13]. By employing this wide distribution, we were able to compare the INCS results for a polydisperse population with those obtained from the effective medium theory of isotropic scatterers [16]. Moreover, this distribution had a mean of  $\mu = ab = 2.76 \mu\text{m}$ , which was close to the radius of the bubbles that resonated at the excitation frequency. In this way, the polydisperse population contained considerable amounts of bubbles that were below resonance, close to resonance and above resonance.

In practice, the range of the  $R_0$  in a polydisperse population is limited [11,13]. In this paper, we considered bubbles with equilibrium radius between  $R_{0,min} = 0.5 \mu\text{m}$  and  $R_{0,max} = 15 \mu\text{m}$ , as depicted in Figure 2. The total density of the MBs considered was (eqn [10]):

$$n_{tot} = \int_{R_{0,min}}^{R_{0,max}} n(R_0) dR_0 \quad (10)$$

Discarded MBs accounted for 4% of the concentration and 0.9% of the gas volume of an un-truncated population.

#### Types of monodisperse and polydisperse suspensions

To make a comparison between the efficiency of a population of monodisperse and polydisperse MBs, we considered four distinct populations:

1. A monodisperse population of MBs with an  $R_0 = 4 \mu\text{m}$  and a resonance frequency ( $f_{res}$ ) = 0.8 MHz (below the center excitation frequency);
2. A monodisperse population of MBs with an  $R_0 = 3.2 \mu\text{m}$  and a  $f_{res} = 1 \text{ MHz}$  (at the center excitation frequency);
3. A monodisperse population of MBs with an  $R_0 = 1 \mu\text{m}$  and a  $f_{res} = 3.9 \text{ MHz}$  (above the center excitation frequency);
4. A polydisperse population of MBs with an  $R_0$  between  $R_{0,min} = 0.5 \mu\text{m}$  and  $R_{0,max} = 15 \mu\text{m}$ , distributed as described in the ‘Configuration for validation’ section and corresponding to a  $f_{res}$  between  $f_{res} = 0.3 \text{ MHz}$  and 10 MHz (a number of MBs were near the  $f_{res}$ , others were above or below resonance).

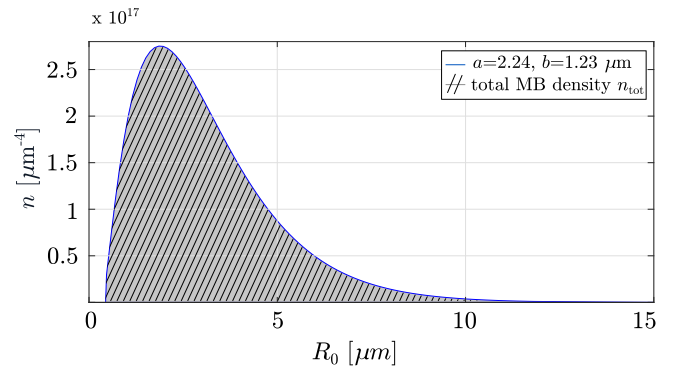


**Figure 2.** Graph depicting continuous gamma distribution with  $\alpha = 2.24$  and  $b = 1.23 \mu\text{m}$  (blue). For  $R_{0,min} = 0.5 \mu\text{m}$  and  $R_{0,max} = 15 \mu\text{m}$ , the area below the curve yielded a concentration of approximately  $n_{tot} = 10^6 \text{ mL}^{-1}$ .

In our simulations, we used high driving pressures to activate the non-linear oscillatory behavior of the MBs and therefore the impact of shell stiffness became unimportant. As a result, the  $f_{\text{res}}$  of the MBs shifted toward the  $f_{\text{res}}$  of an uncoated bubble [2], which was different from the  $f_{\text{res}}$  of a linearly oscillating MB with a shell. As explained in detail by Overvelde et al. [34], we could therefore approximate the  $f_{\text{res}}$  by the eigenfrequency (eqn [11]):

$$f_{\text{res}} = \frac{1}{2\pi R_0} \sqrt{\frac{1}{\rho_0} \left[ 3\gamma P_{\text{amb}} + (3\gamma - 1) \frac{2\sigma\omega}{R_0} \right]}, \quad (11)$$

where  $R_0$  is the  $R_0$  of the MB,  $\gamma = 1.07$  is the polytropic exponent of the gas encapsulated in the bubble,  $P_{\text{amb}} = 101.3$  kPa is the static ambient pressure and  $\sigma_\omega = 0.072$  N/m is the surface tension of the gas-water interface. The center excitation frequency  $f_0 = 1$  MHz corresponded to an  $f_{\text{res}}$  of an uncoated MB of  $R_0 = 3.2$   $\mu\text{m}$ .

For solving the Marmottant equation [4], we further used the gas core viscosity  $\mu = 2 \times 10^{-3}$  Pa·s, effective surface tension  $\sigma(R) = 0.036$  N/m and shell elasticity  $\chi = 0.4$  N/m [13,14]. The surface dilatational viscosity of the shell was given by  $\kappa_s = 1.5 \times 10^{-9} \exp(8 \times 10^5 R_0)$  kg/s, which approximates the data shown in Figure 6B in [35]. Thus, the oscillatory behavior and the frequency spectrum of a single MB when excited with a driving pressure  $P_0 = 200$  kPa and a center frequency  $f_0 = 1$  MHz is depicted in Figure 3.

### Simulation of CEUS imaging

To actually see the difference between monodisperse and polydisperse populations for contrast-enhanced imaging, it was necessary to visualize the reconstructed beam-formed images from the scattered radiofrequency data generated by a realistic configuration. To mimic

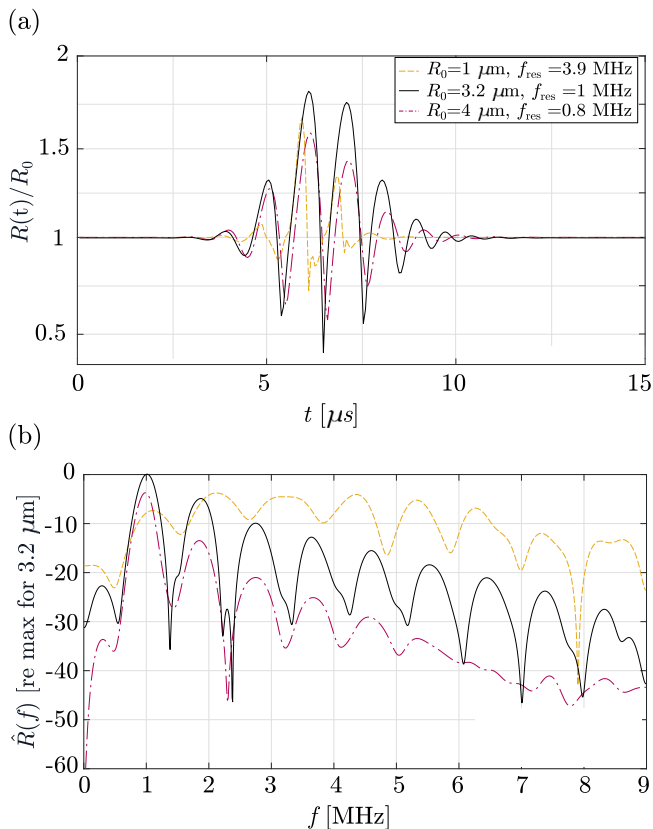


**Figure 3.** (a) Temporal radial responses  $R(t)$  of microbubbles with rest radii of 1  $\mu\text{m}$  (dashed orange), 3.2  $\mu\text{m}$  (black continuous) and 4  $\mu\text{m}$  (dotted purple) when excited by a three-cycle pulse with 200 kPa peak pressure and 1 MHz center frequency. (b) The frequency spectra  $\hat{R}(f)$  corresponding to the signals in (a).

tissue with an enclosed vessel, we distributed LSs surrounding a cylindrical population of MBs, as depicted in Figure 1b. We needed to take into account all of the relevant phenomena that would occur during the propagation of ultrasound through the populations of scatterers inside the water background medium. Based on this, the new non-linear wave equation was given by eqn (12):

$$c_0^{-2} \partial_t^2 p - \nabla^2 p = S_{\text{pr}} + S_{\text{MBs}}(p) + S_{\text{LSs}}(p) + S_{\text{nl}}(p) + S_{\text{v}}(p), \quad (12)$$

where  $S_{\text{MBs}}$  is the contrast source term for the MB population [26],  $S_{\text{LSs}}$  is the contrast source term for the LS population [26], and  $S_{\text{nl}}$  and  $S_{\text{v}}$  are the terms for global [26] and local medium non-linearities [32], respectively. A description of each source term is given in Appendix A. Eqn (12) is solved iteratively using a Neumann scheme, as described in previous publications [26,36].

The incident pressure field was computed for a P4-1 probe (Verasonics, Washington, WA, USA). Transducer elements were height  $H_{\text{ei}} = 16$  mm, width  $W_{\text{ei}} = 0.245$  mm and pitch  $D_{\text{tr}} = 0.295$  mm. The emitted pressure field was approximately a plane wave, with a time signature as given by eqn (5). The center frequency was  $f_0 = 2.5$  MHz and the peak pressure at the transducer surface was  $P_0 = 200$  kPa to activate the non-linear behavior of the monodisperse MBs. Next, the domain of the MB population was a cylinder with center  $(x, y, z) = (0, 0, 22.5)$  mm, diameter of 5 mm and length of 10 mm, as illustrated in Figure 1 (b). This corresponded to a total volume of 0.2 mL. The domain of LSs surrounding the MBs was a cube of  $X \times Y \times Z = 8$  mm  $\times$  10 mm  $\times$  12 mm, corresponding to a volume of 0.76 mL centered at  $(x, y, z) = (0, 0, 24)$  mm, as depicted in Figure 1b. Furthermore, the background medium was water with a co-efficient of non-linearity of  $\beta = 3.21$  (see eqn [A.4] in Appendix A).

To accurately solve the full non-linear wave equation up to the second harmonic frequency ( $h = 2$ ) of the incident pressure pulse, we needed a Nyquist frequency of at least  $F_{\text{nyq}} = (h + 1.5)f_0 = 3.5f_0$ . To also safely capture the higher harmonics of the MB scattering, we used  $F_{\text{nyq}} = 5f_0 = 12.5$  MHz. Thus, the sampling frequency, used for discretizing the spatiotemporal domain, was  $F_s = 2F_{\text{nyq}} = 25$  MHz. Furthermore, we needed at least  $j = h + 1 = 3$  iterations for an accurate prediction of the second harmonic [28]. We took  $j = 10$  iterations to ensure that the relative root mean square error between successive iterations was below  $10^{-6}$ . This also implied that our simulations accounted for MB interactions up to ninth-order multiple scattering [26].

We compared CEUS imaging with two different MB populations:

1. A resonant monodisperse population of MBs with an  $R_0 = 1.4$   $\mu\text{m}$  and a  $f_{\text{res}} = 2.5$  MHz (at the center excitation frequency);
2. A polydisperse population of MBs with an  $R_0$  between  $R_0 = 0.5$   $\mu\text{m}$  and 15  $\mu\text{m}$ , distributed as described in the ‘Configuration for validation’ section, and a  $f_{\text{res}}$  between  $f_{\text{res}} = 0.3$  and 10 MHz.

Each LS has a scattering strength that could be computed through eqn (A.3) in Appendix A, for a polydispersity co-efficient  $f = 1$ .

For the beamforming process, we used the MUST [37] toolbox after employing the amplitude modulation (AM) technique and a virtual point source formulation, as described by Garcia et al. [38].

## Numerical results

### Comparison of INCS and effective medium theory

In this section, we assumed that there were  $N = 10^6$  MBs located in the  $V = 1$  mL volume indicated in Figure 1a. The suspension had a type 4 polydisperse distribution, as described in the ‘Types of monodisperse and polydisperse suspensions’ section. The total gas volume corresponded to  $2.38 \times 10^{-4}$  mL. It was assumed that the gas inside the bubbles was  $\text{C}_4\text{F}_{10}$ , with a density of  $\rho_1 = 10$  kg/m<sup>3</sup> and a speed of sound of  $c_1 = 100$  m/s. As we wanted to perform a simplified comparison with

effective medium theory, we did not take into account the  $f_{\text{res}}$  and the non-linear behavior of the MBs. Instead, we assumed that each bubble could be described by its scattering behavior as described in Eqs. (A.3) to (8). In other words, we were only interested on the scattered signal of each point scatterer. The maximum of the incident pressure  $P_0 = 200$  kPa did not affect the final result as we operated in the linear regimen.

According to Foldy's theory [16,17], the effect of a polydisperse population of scatterers is represented by replacing the wave number,  $k_0$ , in the scattering domain by a corrected wave number,  $k$ , according to eqn (13):

$$k^2 = k_0^2 + 4\pi \int_{R_{0,\min}}^{R_{0,\max}} g(R_0, \omega) n(R_0) dR_0 \quad (13)$$

where  $g(R_0, \omega)$  [m] is derived from eqn (8) and  $n(R_0)$  is computed through eqn (9). The shift in wavenumber corresponds to a shift in wave speed and, as a consequence, in a time shift of the wave that has traversed the scattering domain. In the case considered in this sub-section, the integral amounted to  $2.3 \times 10^5 \text{ m}^{-2}$ . This yielded a wave speed of 1375.5 m/s in the scattering domain, while the speed in the medium without scatterers was 1482 m/s. As the scattering domain had a length of 4.4444 mm, the additional time delay caused by the scattering domain, as predicted by the theory of Foldy, was  $\Delta t_{\text{Foldy}} = 0.228 \mu\text{s}$ . We also determined the time delay between the incident wave,  $p^{(0)}$ , and the wave with all significant orders of scattering,  $p^{(8)}$ , from Figure 4 by looking at the shift in the zero crossings at approximately  $13 \mu\text{s}$ . This was found to be  $\Delta t_{\text{NCS}} = 0.232 \mu\text{s}$ . Thus, the difference in time delay, as predicted by the theory of Foldy and our method, was only 1.75%.

Furthermore, as the wave number derived from eqn (13) lacked an imaginary component in our specific case, according to Foldy's theory [16,17] the wave traversing the scattering domain was not subject to attenuation. As illustrated in Figure 4, in our approach the later iterations corrected the larger amplitudes observed in earlier iterations, and iteration  $p^{(8)}$  had the same amplitude as the incident field  $p^{(0)}$ . This consistency in both time delay and wave amplitude across a scattering domain indicates a good quantitative agreement between our method and Foldy's effective medium theory in case of a polydisperse distribution of scatterers.

#### Plane wave: monodisperse versus polydisperse populations

We continued with a comparison between four different populations of MBs, as mentioned in the section 'Types of monodisperse and polydisperse suspensions.' To start, our reference was the type 2 monodisperse resonant population, for which we used 35,000 MBs, resulting in a total gas volume of  $4.8 \times 10^{-6}$  mL. To achieve a fair comparison, the total gas volume concentration of the MB suspension needed to be the same in all cases [26]. Therefore, the type 1 monodisperse population included 17,920 MBs, the type 3 monodisperse population included about  $10^6$

MBs (1,146,880 MBs) and the type 4 polydisperse population included 20,000 MBs. MB populations were placed in the volume  $V = 1$  mL, as indicated in Figure 1a.

#### Scattered pressure field: full spectrum

The scattered pressure field in each case is depicted in Figure 5. At first sight, the scattered pressure generated from the resonant MBs (type 2,  $R_0 = 3.2 \mu\text{m}$ ) was strongest between all cases, with a peak pressure of +1.1 dB relative to the peak incident pressure  $P_0$ . Next, the case below resonance (type 1,  $R_0 = 4 \mu\text{m}$ ) followed, with a relative peak amplitude of -1.13 dB. Although these MBs had a pressure-dependent  $f_{\text{res}}$  that was still close to the excitation frequency, their peak amplitude was significantly smaller than the resonant MBs. The third case with a relative peak amplitude of -1.45 dB was the case above resonance (type 3,  $R_0 = 1 \mu\text{m}$ ) and the last case was polydisperse distribution (type 4), with a peak pressure of -5.47 dB. These results demonstrate that when the pressure-dependent  $f_{\text{res}}$  was closer to the excitation frequency, then the scattered pressure field was stronger, with scattering of the resonant contrast agents being the highest. Another observation was that the beam profile was smoother if the bubbles were smaller. This is because more MBs were necessary to achieve the same gas volume concentration and the higher the number of scatterers gave a smoother beam profile of the scattered field. Finally, as the incident wave propagated through every MB population, it underwent attenuation and speed of sound variations that were inter-related with a pressure-dependent shift of the MB  $f_{\text{res}}$  [7].

#### Scattered pressure field: harmonics

Here we looked at the different harmonics of the excitation pulses present in the scattered pressure field. These were obtained by decomposing the scattered signal into specific frequency bands using a fourth-order Butterworth filter. These frequency bands were (i) the fundamental ( $F_0$ ) [0.7, 1.3] MHz, (ii) the second-harmonic 2H [1.7, 2.3] MHz and (iii) the third-harmonic 3H [2.7, 3.3] MHz, where the intervals defined the cutoff frequencies of the applied filter.

Figure 6 shows the harmonic contributions of the scattered pressure field for each of the considered populations. In the fundamental ( $F_0$ ) frequency band (Fig. 6, top row), we observed that the strongest scattered field was generated by the type 2 resonant MB suspension with a peak amplitude of -1.23 dB. The type 1 population with below-resonance oscillating MBs had the second highest peak pressure of -2.61 dB as the  $f_{\text{res}}$  was closer to the excitation frequency in comparison to the other two remaining cases. A significant observation was that the scattered field from the type 4 polydisperse population had a peak amplitude of -7.1 dB and was stronger than the case of type 3 above-resonance MBs, which had a peak pressure of -8.74 dB. This could be explained due to the presence of MBs with a  $f_{\text{res}}$  of around 1 MHz in the polydisperse suspension.

In the second harmonic (2H) frequency band (Fig. 6, middle row), we observed that the scattered field of the type 2 resonant MBs was still the highest of all four distinct cases. The peak amplitude in this case was -10.3 dB. The peak pressure of the type 3 above-resonance oscillating MBs was -12.09 dB, which was larger than the respective value of -15.82 dB of the type 1 population with the below-resonance oscillating MBs. This could be explained by the fact that the  $f_{\text{res}}$  of the system of the former was closer to the 2H frequency band at around 2 MHz. The type 4 polydisperse distribution showed the weakest peak pressure amplitude at -18.89 dB. Compared with monodisperse populations, hardly any constructive interferences were observed below the polydisperse suspension due to the varying oscillation phases that resulted from differing contrast bubble sizes.

Finally, for the third harmonic (3H) frequency band (Fig. 6, bottom row), the type 3 below-resonance MBs exhibited the strongest scattered pressure field with a peak amplitude of -17.49 dB, as their  $f_{\text{res}}$  of 3.9 MHz was closer to the 3H frequency band. Additionally, type 2 resonant MBs scattered the second highest pressure field with a peak

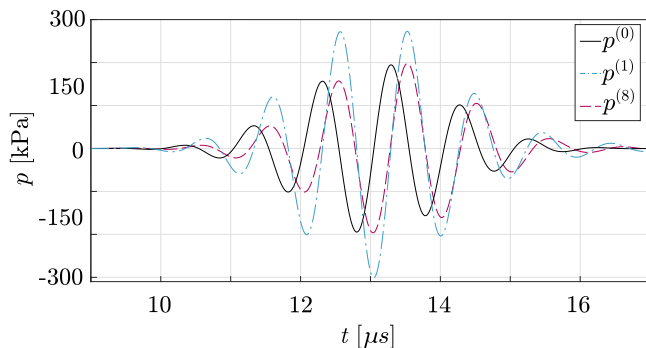


**Figure 4.** Comparison between time signatures of the incident pressure pulse ( $p^{(0)}$ , black continuous line) and the total pressure pulse after  $j = 1$  ( $p^{(1)}$ , blue dotted line) and  $j = 8$  ( $p^{(8)}$ , magenta dashed line) iterations that are received by a point receiver located on the  $z$ -axis at  $z = 10.3$  mm.

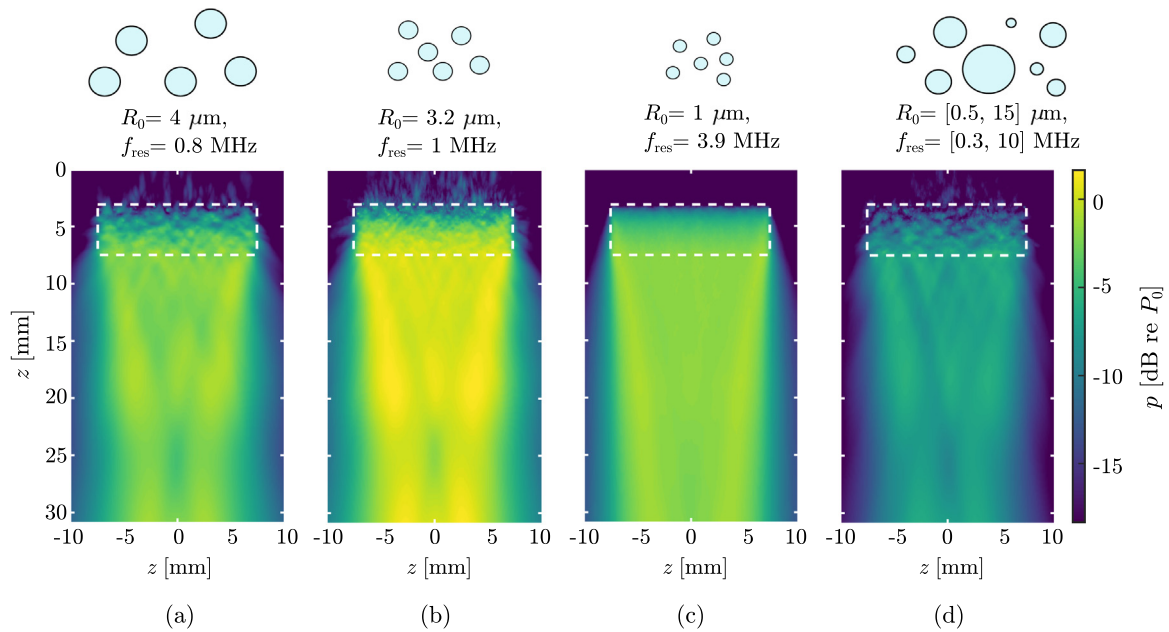


**Figure 5.** Peak of the total scattered pressure at  $y = 0$  mm for (a) a type 1 monodisperse distribution of microbubbles (MBs), (b) a type 2 monodisperse distribution of MBs, (c) a type 3 monodisperse distribution of MBs and (d) a type 4 polydisperse distribution of MBs. In all four cases, the population was located inside the dashed white rectangle.

amplitude of -18.49 dB. Within the MB suspension, type 4 polydisperse MBs gave a peak pressure of -22.66 dB. This was stronger than the peak of the pressure field of the type 1 below-resonance oscillating MBs (-25.91 dB), as smaller MBs with an  $f_{\text{res}}$  close to 3 MHz added to the strong scattering of the larger MBs. Similar to 2H, type 4 polydisperse MBs hardly yielded constructive interference below the suspension, as was the case for type 1, 2 and 3 monodisperse MBs. This observation predicts that the uniformity of the size distribution of a population could have an impact on non-linear imaging artifacts downstream of the population.

The cumulative scattered pressure field comprised the addition of signals emitted from all MBs in the population considering their individual position and therefore all phase delays. A simplified expression linearly projected the behavior of a single MB onto the behavior of an entire population of MBs. Thus, simulated population pressure fields showed similar behavior to the projected response of the single MB shown in Figure 3.

#### Total pressure field: attenuation and speed of sound variations

To demonstrate the influence of non-linear MB behavior on a propagating pressure wave, Figure 7 shows the temporal signatures and respective frequency spectra after traversing each type of MB population. In Figure 7a it is clear that the type 2 monodisperse resonant population (black line) caused the most non-linear distortion, which took place mainly after the second cycle as the MBs needed to achieve a large oscillation amplitude before they could demonstrate significant non-linear behavior. The influence of non-linear bubble oscillation on propagation through each of the other three populations is much less visible in the time domain. By observing the frequency spectra in Figure 7b, we were able to better see the effect of non-linear bubble behavior. Similar to the section ‘Scattered pressure field: harmonics,’ type 2 monodisperse oscillating MBs showed a shift in energy from fundamental to second and higher harmonics. Furthermore, the maximum spectral amplitude of the fundamental was approximately equal for the other population types. The type 3 population of monodisperse below-resonance MBs showed a strong second harmonic and the highest third harmonic of all populations, even higher than type 2.

To quantify the attenuation and speed of sound changes in the fundamental frequency band, subjected the temporal signatures in Figure 7a

were subjected to an eighth-order Butterworth filter and a [0.75, 1.25] MHz frequency pass band. The results are plotted in Figure 8. For the type 1 MB population that was below resonance, a decrease in peak pressure of 92.2 kPa occurred relative to the incident field, with the speed of sound increasing to 1517 m/s. For the type 2 MB population with resonant bubbles, the peak pressure underwent a drop of 126.9 kPa and the speed of sound was maintained at 1482 m/s. For the type 3 MB population that was above resonance, peak pressure experienced a drop of 19.9 kPa and the speed of sound decreased to 1458 m/s. Finally, for the type 4 polydisperse MB population, there was a decay in peak pressure by 44.8 kPa and the speed of sound increased to 1497 m/s. We observed that the differences for type 3 MBs were the smallest of all populations because they presented the strongest effect, mainly on the second harmonic. As shown in previous studies [7], INCS simulations demonstrate that for MBs with a  $f_{\text{res}}$  below the excitation frequency there is an increase in wave speed, whereas for a resonance higher than the excitation frequency there is a decrease in wave speed. Finally, for MBs with a  $f_{\text{res}}$  equal to the excitation frequency, the wave speed is equal to the speed of sound of the background medium.

#### Total pressure field: convergence behavior

To quantify the numerical performance of our scheme, we analyzed the difference between successive iterations using the relative root mean square error (RRMSE) (eqn [14]):

$$\text{RRMSE} = \sqrt{\frac{\int_{X_{\text{cd}}} \int_{T_{\text{cd}}} [p^{(j)}(\mathbf{x}, t) - p^{(j-1)}(\mathbf{x}, t)]^2 dt d\mathbf{x}}{\int_{X_{\text{cd}}} \int_{T_{\text{cd}}} [p^{(0)}(\mathbf{x}, t)]^2 dt d\mathbf{x}}}, \quad (14)$$

where  $X_{\text{cd}}$  is the spatial computational domain,  $T_{\text{cd}}$  is the temporal computational domain,  $j$  is the iteration number and  $p^{(j)}$  is the total pressure obtained in the  $j$ th iteration. The decay of the RRMSE is illustrated in Figure 9 as a function of the number of iterations. An initial observation was that after a certain number of successive iterations, the error tended to stabilize at a level of  $10^{-5}$  or below. At this juncture, it could be inferred that incorporating additional multiple-scattering orders would not yield further enhancements to the solution, indicating the attainment of insignificant scattering orders. Upon reaching this stage, it was assumed that the iterative process had converged to the lowest achievable error.

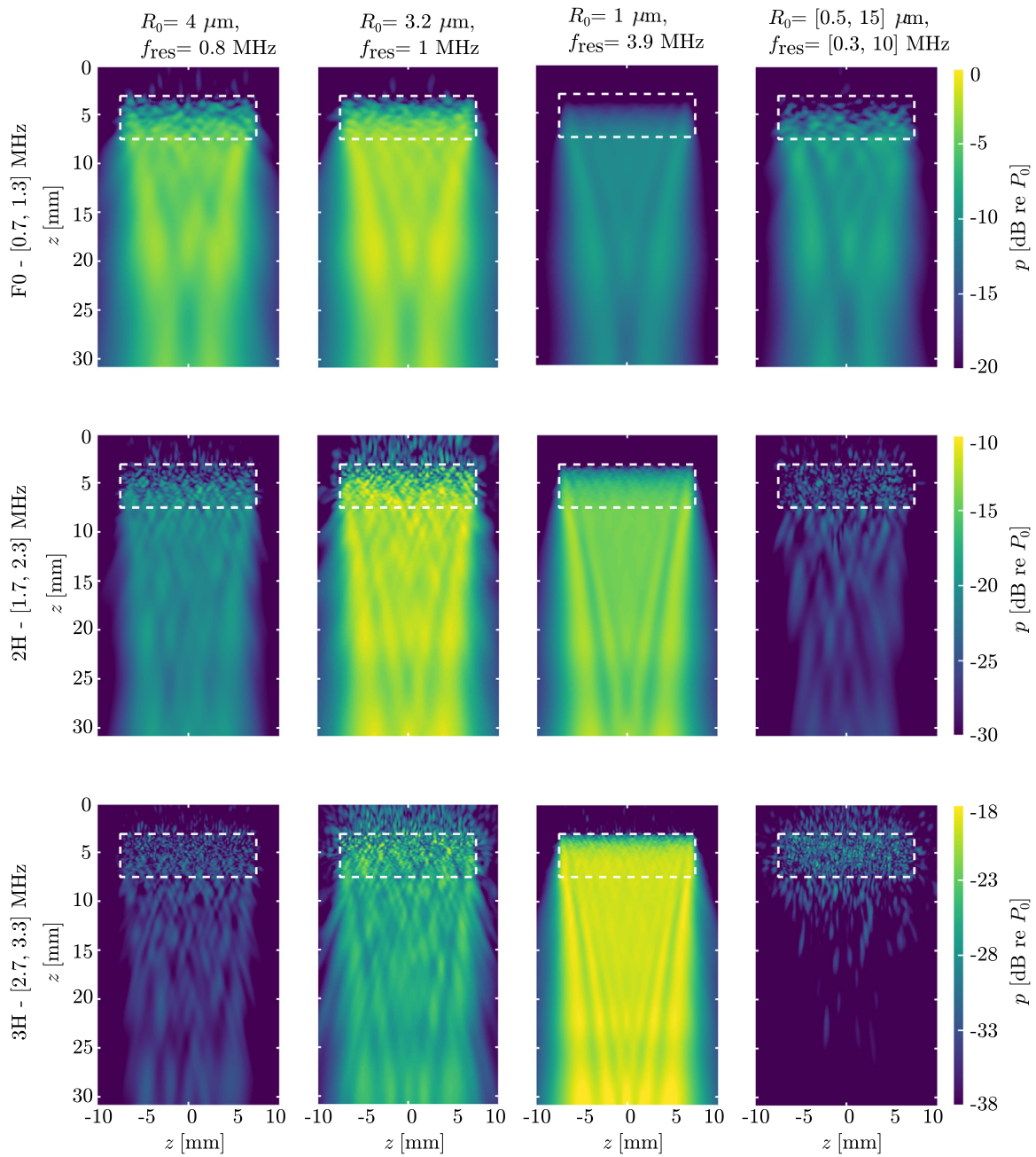


**Figure 6.** Peak of the scattered pressure at  $y = 0$  mm for: (first column) a type 1 monodisperse distribution of microbubbles (MBs), (second column) a type 2 monodisperse distribution of MBs, (third column) a type 3 monodisperse distribution of MBs and (fourth column) a type 4 polydisperse distribution of MBs. Each row corresponds to a specific frequency band: (first row) fundamental  $F_0$  [0.7, 1.3] MHz, (second row) second-harmonic 2H [1.7, 2.3] MHz and (third row) third-harmonic 3H [2.7, 3.3] MHz. In all four cases, the population was located inside the dashed white rectangle.

For type 2 monodisperse resonant MBs, it was shown that the initial iterations showed an RRMSE above 1, which indicates that the first multiple-scattering orders were highly significant. Moreover, for these MBs more iterations were needed to reach convergence, and therefore more multiple-scattering orders needed to be included to achieve an accurate result. A general observation is that the closer the  $f_{res}$  of the population is to the excitation frequency, the more iterations need to be considered. This can be explained by the fact that stronger close-range interactions occur in populations with resonant MBs due to the stronger scattering strength, making higher scattering orders more important. By observing the case of type 3 above-resonance monodisperse MBs, the RRMSE of the initial iterations was also above 1. This was due to the larger number of scatterers used to achieve the same gas volume concentration, which

corresponded to a higher number of bubble-bubble interactions at short distances. Finally, type 4 polydisperse MBs yielded faster convergence (in the 13th iteration) than any other type of monodisperse suspension, demonstrating the relative significance of multiple scattering in monodisperse populations.

#### CEUS imaging

##### Scattered pressure fields

In this section we compared non-linear scattering coming from suspensions of type 5 resonant monodisperse MBs and type 6 polydisperse MBs when these were surrounded by LSs, as illustrated in Figure 1b. To resemble an *in vivo* setting and match the gas volume concentration, for

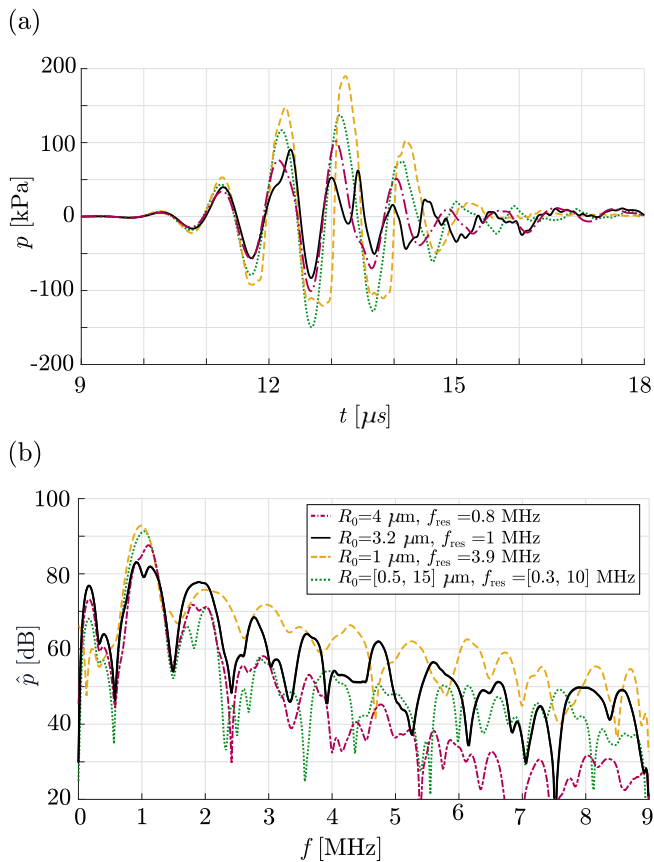


**Figure 7.** (a) Temporal signature and (b) frequency spectra of the total pressure field after propagation through each of the four distinct MB populations. Pressure was obtained for a point receiver located on the z-axis at a depth of  $z = 10.3$  mm.

the type 5 suspension we used a concentration of  $5 \times 10^5 \text{ mL}^{-1}$  MBs with a  $1.4 \mu\text{m}$   $R_0$ , corresponding to a total gas volume of  $5.8 \times 10^{-6}$  mL. Furthermore, for type 6 we used  $3.1 \times 10^4 \text{ mL}^{-1}$  MBs, corresponding to the same total gas volume. First, the total pressure fields in these configurations were computed for three different excitations: field  $p_1$  was due to a double-amplitude excitation (full aperture), and fields  $p_2$  and  $p_3$  resulted from two single-amplitude excitations (odd and even elements), respectively. After employing the AM procedure, the peak residual AM pressures were as shown in Figure 10. For the monodisperse case in Figure 10a, non-linear effects accumulated in the suspension and propagated in the area below the population. The peak AM residual pressure was  $-3.7$  dB relative to the pressure at the source surface,  $P_0$ . On the other hand, for the polydisperse case in Figure 10b, the residual pressure field showed a relative peak amplitude of  $-19.9$  dB, which was 6.5 times smaller than the residual pressure field due to the monodisperse suspension. Most MBs in the polydisperse suspension were less efficient scatterers than resonant monodisperse population MBs. More importantly, bubbles of different sizes caused non-linear scattering at different phases, meaning that the non-linearities caused by scattering did not propagate outside the MB domain. These results indicate that in CEUS, non-linear wave-propagation artifacts are stronger for a resonant monodisperse population than a polydisperse population.

To demonstrate what this meant for the AM imaging process, in Figure 11 we compared the time signatures of the double-amplitude pulse,  $p_1$ , the sum,  $p_2 + p_3$ , of the two single-amplitude pulses and the AM residual,  $p_1 - (p_2 + p_3)$ , for both type 5 monodisperse and type 6 polydisperse cases. These temporal signatures are depicted for the center of the aperture of the linear array.

In Figure 11a, the AM residual of the monodisperse population was a strong signal with a peak pressure of 1.5 kPa, compared with 2.11 kPa

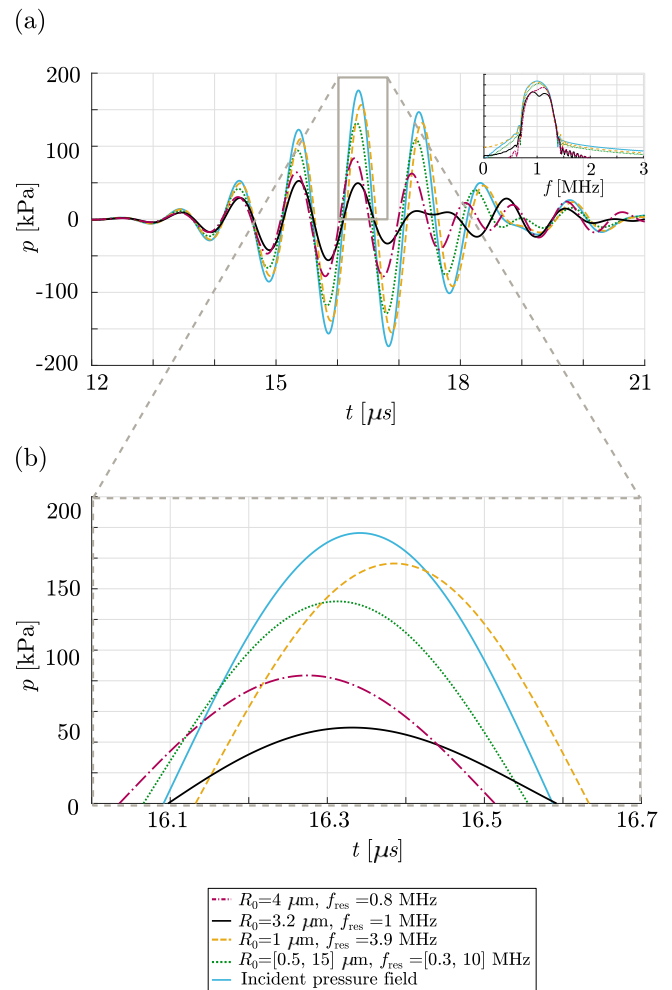


**Figure 8.** (a) Temporal signature of the total pressure field in the fundamental frequency band after propagation through each of the four distinct microbubble populations. (b) Magnified version of (a) demonstrating the attenuation and speed of sound changes of the transmitted wave. The pressure was obtained for a point receiver located on the z-axis at a depth of  $z = 10.3$  mm.

for the incident double-excitation field. The sum of the two single-amplitude signals matched the waveform of the double-amplitude signal only for smaller time instants, which corresponded to LS scattering that was present above the MB suspension. The AM residual signal was stronger for larger time instants, which indicates the propagation of non-linear MB scattering to the LSs located below the MB suspension.

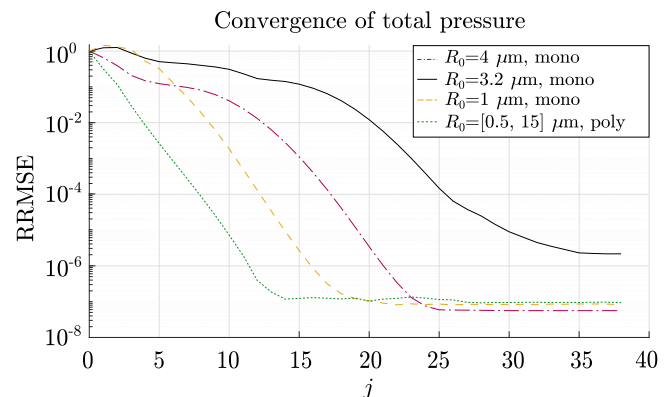


**Figure 9.** Relative root mean square error as a function of the number of iterations,  $j$ , for the considered microbubble population types.

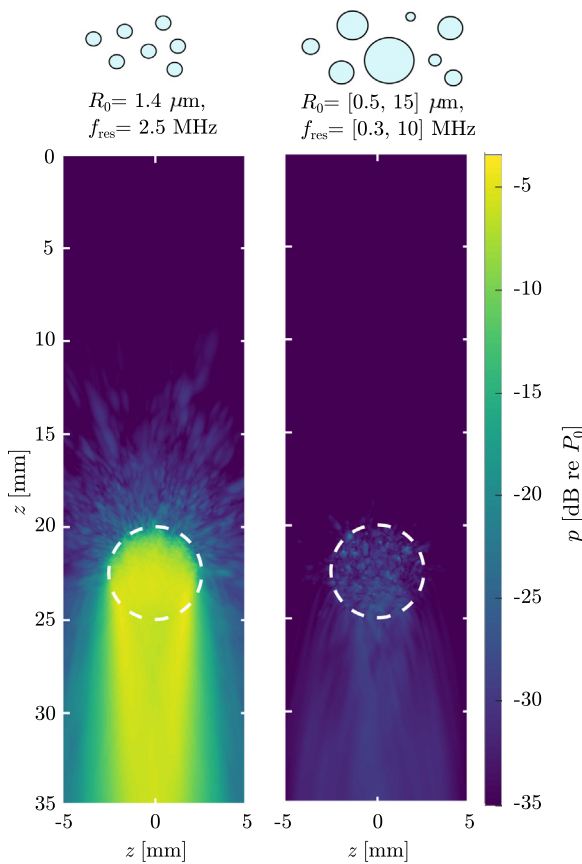


**Figure 10.** Residual acoustic pressure fields after the amplitude modulation operation in the presence of (a) a type 5 resonant monodisperse population and (b) a type 6 polydisperse population. The microbubbles are located inside the dashed white circle.

In contrast, **Figure 11b** shows that in the polydisperse case, the peak pressure of the AM residual corresponded to 0.35 kPa, which was 4.3 times smaller than the respective value of the type 5 monodisperse population. Moreover, the sum of the single-amplitude signals overlapped with the double-amplitude signal, both for smaller time instants (scattering from the LSs above the MB suspension) and for larger time instants (scattering from the LSs below the MB suspension). This indicates that the non-linear scattering that propagated below the polydisperse MB suspension was relatively small.

#### Effect of size distribution on imaging artifacts

To assess the imaging effects of the non-linear fields below each MB population, it was necessary to generate the reconstructed B-mode (single-shot) images as well as the images that were obtained after employing the AM procedure. The results are depicted in **Figure 12**. To achieve this, we placed  $7 \times 10^5 \text{ mL}^{-1}$  tissue-mimicking LSs (gray) around the MB suspension.

**Figure 12** (a, b) depicts B-mode images for the configuration with a resonant monodisperse MB population and a polydisperse population, respectively. In both cases the backscattering from tissue-mimicking LSs and MBs was indistinguishable as the areas with LSs and MBs had a similar echogenicity, independent of size distribution. This demonstrates that B-mode imaging does not allow disentanglement of non-linear MB scattering from tissue-mimicking scattering.

**Figures 12** (c, d) shows AM images for the configuration with a resonant monodisperse MB population and a polydisperse population, respectively. Employing the AM sequence for imaging a monodisperse MB population generated an image with significant non-linear artifacts below the MB area, meaning that tissue scatterers were misclassified as

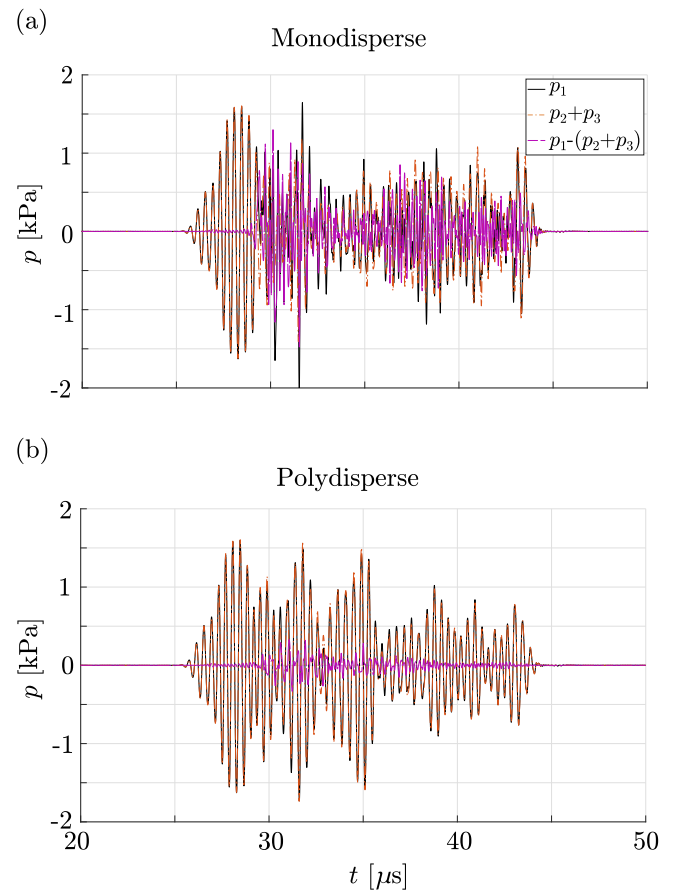


**Figure 11.** Temporal signatures used in the amplitude modulation (AM) procedure for (a) type 5 monodisperse resonant and (b) type 6 polydisperse populations, both surrounded by tissue-mimicking linear scatterers and measured at the center of the aperture of the linear array. Each of these graphs encompasses three plots representing the double-amplitude signal,  $p_1$ , the sum of the two respective single-amplitude signals,  $p_2 + p_3$ , and the AM residual signal,  $p_1 - (p_2 + p_3)$ .

MBs. Conversely, applying the AM sequence to image the polydisperse population delivered an image with much higher specificity. The peak amplitude of the monodisperse area image (0 dB) was stronger than in the polydisperse area image (−11.8 dB). The peak value of the non-linear artifact level was −10.04 dB for the monodisperse population and −29.4 dB for the polydisperse population. This is an indication that monodisperse MBs are more efficient scatterers than polydisperse populations, especially in applications that require enhanced deep tissue imaging. A drawback of CEUS with monodisperse MBs is that the artifacts generated from the propagation of non-linear scattering in the area below the MBs is of comparable magnitude and could lead to the misclassification of tissue as contrast agents.

#### Conclusion

We simulated AM ultrasound imaging of both monodisperse and polydisperse MBs using the INCS method, taking into account all the relevant physical phenomena occurring during ultrasound propagation through a MB population. We also highlighted the significance of multiple scattering in monodisperse populations. Resonant monodisperse MBs were shown to be the most efficient scatterers, which corresponded to high sensitivity for CEUS. This property is crucial for optimizing contrast enhancement and guaranteeing consistent behavior and reliable imaging outcomes, especially compared with using polydisperse contrast agents. The drawback of resonant monodisperse MBs is the generation of imaging artifacts, which reduce the specificity of CEUS. This

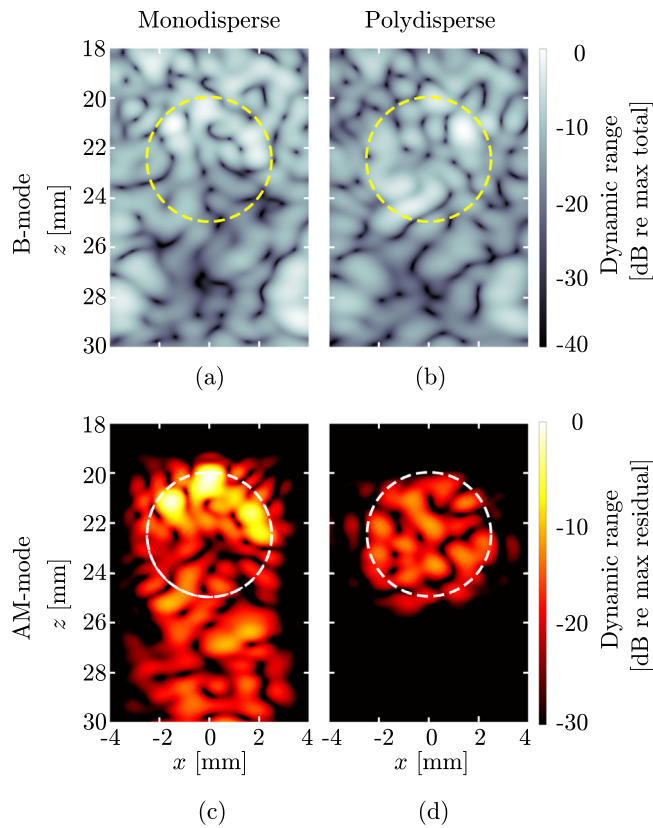


**Figure 12.** B-mode and amplitude modulation (AM)-mode images of the monodisperse microbubble (MB) population and its surrounding region. B-mode (single-shot) ultrasound images were acquired for a region with (a) a type 5 monodisperse resonant population and (b) a type 6 polydisperse MB population. AM ultrasound images were acquired for the same regions of (c) monodisperse and (d) polydisperse MB populations. The position of the MB populations is outlined by a dashed circle. The rest of the simulation domain is filled with tissue-mimicking linear scatterers.

research approach was useful for optimizing CEUS imaging by designing the size distribution and parameters of an MB population through simulations.

#### Conflict of interest

The authors declare no competing interests.

#### Acknowledgments

This research was supported by the ‘Optoacoustic sensor and ultrasonic MBs for dosimetry in proton therapy’ project of the Dutch National Research Agenda, partly financed by the Dutch Research Council (NWO). The authors thank N. de Jong for his involvement in this research.

#### Data availability

The data that support the findings of this study are available from the corresponding author upon reasonable request.

#### Declaration of generative AI and AI-assisted technologies in the writing process

During the preparation of this work the authors used ChatGPT in order to improve the readability and language of the Abstract, Introduction and Conclusions. After using this tool/service, the authors reviewed

and edited the content as needed and take full responsibility for the content of the publication.

#### Appendix A. Description of source terms in eqn (12)

Primary source that generates the incident field (eqn [A.1]):

$$S_{pr}(\mathbf{x}, t) = \rho_0 \frac{\partial q(\mathbf{x}, t)}{\partial t} - \nabla \cdot \mathbf{f}(\mathbf{x}, t), \quad (\text{A.1})$$

Contrast source representing the scattering of a population of non-linear microbubbles (eqn [A.2]):

$$S_{MBS}(\mathbf{x}, t) = \rho_0 \sum_{i=1}^N \frac{d^2 V^{(i)}(\mathbf{x}_{sc}^{(i)}, t)}{dt^2} \delta(\mathbf{x} - \mathbf{x}_{sc}^{(i)}), \quad (\text{A.2})$$

Contrast source representing the scattering of a population of linear scatterers (eqn [A.3]):

$$S_{LSs}(\mathbf{x}, t) = -\frac{\rho_0}{\rho_1 c_1^2} \sum_{m=1}^M V_0^{(m)} \frac{\partial^2 p(\mathbf{x}_{sc}^{(m)}, t)}{\partial t^2} \delta(\mathbf{x} - \mathbf{x}_{sc}^{(m)}) \quad (\text{A.3})$$

Contrast source representing the non-linear global effects of the embedding medium (eqn [A.4]):

$$S_{nl}(\mathbf{x}, t) = \frac{\beta}{\rho_0 c_0^4} \frac{\partial^2 p(\mathbf{x}, t)^2}{\partial t^2}, \quad (\text{A.4})$$

Contrast source representing the local non-linear effects of the embedding medium (eqn [A.5]):

$$S_{\mathcal{L}}(\mathbf{x}, t) = (\nabla^2 + c_0^{-2} \partial_t^2) \mathcal{L}(\mathbf{x}, t), \quad (\text{A.5})$$

in which (eqn [A.6]):

$$\mathcal{L}(\mathbf{x}, t) = \frac{1}{2} \rho_0 v^2(\mathbf{x}, t) - \frac{1}{2} \kappa_0 p^2(\mathbf{x}, t), \quad (\text{A.6})$$

is the so-called Lagrangian density, with  $p(\mathbf{x}, t)$  indicating the acoustic pressure and  $v(\mathbf{x}, t)$  indicating the particle velocity.

#### References

- [1] Averkiou M, Bruce M, Powers J, Sheeran P, Burns P. Imaging methods for ultrasound contrast agents. *Ultrason Med Biol* 2020;46(3):498–517.
- [2] Versluis M, Stride E, Lajoinie G, Dollet B, Segers T. Ultrasound contrast agent modeling: A review. *Ultrason Med Biol* 2020;46(9):2117–44.
- [3] de Jong N, Bouakaz A, Frinking P. Basic acoustic properties of microbubbles. *Echocardiography* 2002;19(3):229–40.
- [4] Marmottant P, van der Meer S, Emmer M, Versluis M, de Jong N, Hilgenfeldt S, et al. A model for large amplitude oscillations of coated bubbles accounting for buckling and rupture. *J Acoust Soc Am* 2005;118(6):3499–506.
- [5] Emmer M, Vos HJ, Goertz DE, van Wamel A, Versluis M, de Jong N. Pressure-dependent attenuation and scattering of phospholipid-coated microbubbles at low acoustic pressures. *Ultrason Med Biol* 2009;35(1):102–11.
- [6] Sojahrood A, Falou O, Earl R, Karshafian R, Kolios M. Influence of the pressure-dependent resonance frequency on the bifurcation structure and backscattered pressure of ultrasound contrast agents: A numerical investigation. *Nonlinear Dyn* 2015;80:889–904.
- [7] Sojahrood AJ, Li Q, Haghi H, Karshafian R, Porter TM, Kolios MC. Probing the pressure dependence of sound speed and attenuation in bubbly media: Experimental observations, a theoretical model, and numerical calculations. *Ultrason Sonochem* 2023;95:106319.
- [8] Errico C, Pierre J, Pezet S, Desailly Y, Lenkei Z, Couture O, et al. Ultrafast ultrasound localization microscopy for deep super-resolution vascular imaging. *Nat* 2015;527:499–502.
- [9] Tang M, Eckersley R. Nonlinear propagation of ultrasound through microbubble contrast agents and implications for imaging. *IEEE Trans Ultrason Ferroelectr Freq Control* 2006;53(12):2406–15.
- [10] Lindner JR. Microbubbles in medical imaging: current applications and future directions. *Nat Rev Drug Discov* 2004;3(6):527–32.
- [11] Frinking P, Segers T, Luan Y, Tranquart G. Three decades of ultrasound contrast agents: A review of the past, present, and future improvements. *Ultrason Med Biol* 2020;46(4):892–908.
- [12] Segers T, Jong N, Versluis M. Uniform scattering and attenuation of acoustically sorted ultrasound contrast agents: Modeling and experiments. *J Acoust Soc Am* 2016;140:2506–17.
- [13] Helbert A, Gaud E, Segers T, Botteron C, Frinking P, Jeannot V. Monodisperse versus polydisperse ultrasound contrast agents: *In vivo* sensitivity and safety in rat and pig. *Ultrason Med Biol* 2020;46(12):3339–52.

- [14] Segers T, Kruizinga P, Kok M, Lajoinie G, de Jong N, Versluis M. Monodisperse versus polydisperse ultrasound contrast agents: Nonlinear response, sensitivity, and deep tissue imaging potential. *Ultrason Med Biol* 2018;44(7):1482–92.
- [15] van Elburg B, Deprez J, van den Broek M, De Smedt S, Versluis M, Lajoinie G, et al. Dependence of sonoporation efficiency on microbubble size: An *in vitro* monodisperse microbubble study. *J Control Release* 2023;363:747–55.
- [16] Foldy LL. The multiple scattering of waves. *Phys Rev* 1945;64:107–19.
- [17] Carstensen EL, Foldy LL. Propagation of sound through a liquid containing bubbles. *J Acoust Soc Am* 1947;19:481–501.
- [18] Stride E, Saffari N. Investigating the significance of multiple scattering in ultrasound contrast agent particle populations. *IEEE Trans Ultrason Ferroelectr Freq Control* 2005;52:2332–45.
- [19] Hibbs K, Mari J, Stride E, Eckersley R, Noble A, Tang M. Nonlinear propagation of ultrasound through microbubble clouds: A novel numerical implementation. In: Paper presented at: 2007 IEEE Ultrasonics Symposium Proceedings; 2007. October 28–31.
- [20] Ando K, Colonius T, Brennen C. Numerical simulation of shock propagation in a polydisperse bubbly liquid. *J Acoust Soc Am* 2011;142:596–608.
- [21] Ovenden N, O'Brien J, Stride E. Ultrasound propagation through dilute polydisperse microbubble suspensions. *J Acoust Soc Am* 2017;142:1236–48.
- [22] Vanhille C, Hynynen H. Numerical simulations of the nonlinear interaction of a bubble cloud and a high-intensity focused ultrasound field. *Acoustics* 2019;1:825–36.
- [23] Pinton G, Dahl J, Rosenzweig S, Trahey G. A heterogeneous nonlinear attenuating full-wave model of ultrasound. *IEEE Trans Ultrason Ferroelectr Freq Control* 2009;56:474–88.
- [24] Joshi A, Lindsey B, Dayton P, Pinton G, Muller M. An iterative fullwave simulation approach to multiple scattering in media with randomly distributed microbubbles. *Phys Med Biol* 2017;62:4202–17.
- [25] Haghi H, Sojahrood AJ, Kolios MC. Collective nonlinear behavior of interacting polydisperse microbubble clusters. *Ultrason Sonochem* 2019;58:104708.
- [26] Matalliotakis A, Verweij MD. Computation of ultrasound propagation in a population of nonlinearly oscillating microbubbles including multiple scattering. *J Acoust Soc Am* 2023;153:2209–22.
- [27] Huijssen J. Modeling of nonlinear medical diagnostic ultrasound, PhD Thesis. The Netherlands, Delft University of Technology, <<http://repository.tudelft.nl>>; 2008. [accessed 14 October 2008].
- [28] Huijssen J, Verweij MD. An iterative method for the computation of nonlinear, wide-angle, pulsed acoustic fields of medical diagnostic transducers. *J Acoust Soc Am* 2010;127(1):33–44.
- [29] Demi L. Modeling nonlinear propagation of ultrasound through inhomogeneous biomedical media, PhD Thesis. The Netherlands, Delft University of Technology, <<http://repositoy.tudelft.nl>>; 2013. [accessed 05 March 2013].
- [30] Demi L, Verweij MD, Huijssen J, de Jong N, van Dongen KWA. Attenuation of ultrasound pressure fields described via a contrast source formulation. In: Paper presented at: 2009 IEEE Ultrasonics Symposium; 2009. p. Rome, Italy1590–3.
- [31] Demi L, van Dongen KWA, Verweij MD. A contrast source method for nonlinear acoustic wave fields in media with spatially inhomogeneous attenuation. *J Acoust Soc Am* 2011;129:1221–30.
- [32] Matalliotakis A, Maresca D, Verweij MD. Nonlinear interaction of two cross-propagating plane waves. *arxiv*, 2023. arXiv:2312.00445.
- [33] Abramowitz M, Stegun I. Handbook of mathematical functions: with formulas, graphs, and mathematical tables. Washington, D.C.: Dover Publications; 2013.
- [34] Overvelde M, Garbin V, Sijl J, Dollet B, de Jong N, Lohse M, et al. Nonlinear shell behavior of phospholipid-coated microbubbles. *Ultrasound Med Biol* 2010;36(12):2080–92.
- [35] Segers T, Gaud E, Versluis M, Frinking P. High-precision acoustic measurements of the nonlinear dilatational elasticity of phospholipid-coated monodisperse microbubbles. *Soft Matter* 2018;14:9550–61.
- [36] Matalliotakis A, Waasdorp R, Verweij MD, Maresca D. Impact of wavefront shape on nonlinear ultrasound imaging of monodisperse microbubbles. *Phys Rev Appl* 2023;22:034062.
- [37] Garcia D. Make the most of MUST, an open-source MATLAB UltraSound Toolbox. In: Paper presented at: 2021 IEEE International Ultrasonics Symposium; 2021. September 11–16.
- [38] Perrot V, Polichetti M, Varray F, Garcia D. So you think you can DAS? A viewpoint on delay-and-sum beamforming. *Ultrasonics* 2021;111:106309.